Experimental Analysis of a Particle Separator Design With Full-Field Three-Dimensional Measurements

Daniel D. Borup[1]
Department of Mechanical Engineering,
Stanford University,
Stanford, CA 94305
e-mail: borup@stanford.edu

Christopher J. Elkins
Department of Mechanical Engineering,
Stanford University,
Stanford, CA 94305
e-mail: celkins@stanford.edu

John K. Eaton
Department of Mechanical Engineering,
Stanford University,
Stanford, CA 94305
e-mail: eatonj@stanford.edu

Particle ingestion into turbine engines can cause significant damage through deposition in internal cooling passages. Musgrove et al. proposed a compact particle separator installed between the combustor bypass exit and turbine vane cooling passage inlet. The design had small pressure losses but provided limited particle separation. Its performance has proved difficult to replicate. Borup et al. recently developed a magnetic resonance imaging (MRI)-based technique for full-field, 3D measurements of the mean particle concentration distribution in complex flows. A particle separator based on the Musgrove et al. design was fabricated out of plastic using 3D printing, with the addition of a drain from the collector through which 3% of the total flow was extracted. The separator efficiency was measured at two Reynolds numbers, using water as the working fluid and 33-μm titanium microspheres to represent dust particles. Stokes number was shown to play the dominant role in determining efficiency across studies. MRI was used to obtain the 3D particle volume fraction and three-component velocity fields. The velocity data showed that flow was poorly distributed between the separator louvers, while the collector flow followed the optimal pattern for particle retention. The MRI data revealed that strong swirling flow in the collector centrifuged particles toward the outer wall of the collector and into a partitioned region of quiescent flow, where they proceeded to exit the collector. Future designs could be improved by re-arranging the louvers to produce a more uniform flow distribution, while maintaining the effective collector design. [DOI: 10.1115/1.4047112]

Keywords: fluid dynamics and heat transfer phenomena in compressor and turbine components of gas turbine engines, heat transfer and film cooling, measurement techniques

Introduction

Particle ingestion is a leading cause of service life reduction for aircraft gas turbine engines operating in dusty environments [1]. This issue has increasing financial implications for the industry as commercial airline operations expand in China, the Middle East, and other regions with high levels of airborne dust. Previous experimental studies have involved exposing full engines to dust or volcanic ash and analyzing the resulting damage mechanisms after engine deterioration or failure [2]. One primary damage mechanism that has been identified in several studies is blockage of cooling passages and/or film cooling holes due to deposition of particulate matter [3,4].

A strategy for designing dust-resistant turbine components is to separate particles from the compressor bypass air before the air enters the small internal passages in a blade or vane. Aircraft engines require separators that are lightweight and compact, which prohibits the use of large filters commonly found on land-based turbines or rotorcraft. One common implementation for commercial aircraft is use of an inertial separator design, in which the air accelerates rapidly around one or more bends in the path. Heavy particles, which are unable to follow the strongly accelerating flow, may be collected in a filter or other chamber, or exhausted from the engine with a small amount of discharge air.

Musgrove et al. [5] recently proposed a louver-based particle separator design to be employed just upstream of the first-stage turbine vane coolant passage inlets. A schematic of the design and key design parameters is provided in Fig. 1. The initial design study, carried out entirely using computational fluid dynamics (CFD), indicated that this design could be capable of providing efficient particle separation with minimal pressure losses; the latter feature is important to ensure sufficient cooling capacity for the vanes. However, subsequent experimental studies have shown mixed results for this and other similar designs [6–8]. The design of the particle collector—located at the downstream end of the separator—has been shown to play a critical role in total particle collection. In addition, Musgrove et al. found that the best performance was achieved with a 30-deg louver angle or a variable angle design and with the minimum number of louvers ($N = 8$).

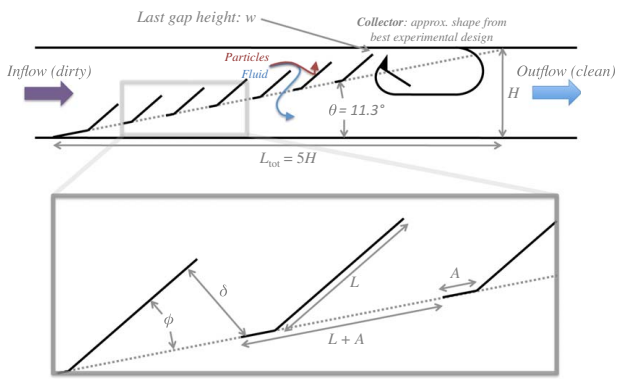

Fig. 1 Design space for louvered particle separator design of Musgrove et al. [5] and others

[1]Corresponding author.

Contributed by the International Gas Turbine Institute (IGTI) of ASME for publication in the Journal of Turbomachinery. Manuscript received January 31, 2020; final manuscript received March 2, 2020; published online September 11, 2020. Assoc. Editor: David G. Bogard.

The large disagreement in predicted performance between simulation and experiments reflects two important issues: first, a limited understanding of the multiphase flow physics inside louvered separators; and second, the lack of sufficient predictive capabilities for multiphase flows using CFD codes. The present study aims to address the lack of reliable experimental data by applying a newly available experimental technique that can provide the full, 3D mean particle concentration distribution for turbulent flows [9–11]. The resulting data provide an improved means for understanding the physics of this particular design, as well as louvered separators in general. The present measurements are also used to suggest design improvements that could help increase separator performance to a level suitable for application in actual engines. Finally, the resulting data set is available upon request for comparison to simulations, allowing for validation of newly developed multiphase CFD codes with improved accuracy.

Experimental Methods

Flow Geometry. The flow model consisted of four sections: (1) a diffuser, (2) a particle injection and mixing section, (3) the louvered separator test section, and (4) an exit contraction. The full geometry is shown in Fig. 2. The main flow entered the diffuser from a 25.4-mm (1 in.) diameter tube and was expanded over 127 mm to a 21.4 × 42.8 mm rectangularcross section. This set the channel height, H, at 21.4 mm for the model separator. A 75% flow blockage grid was included at the downstream end of the diffuser to produce a more uniform flow distribution. Flow proceeded around a NACA 0030 airfoil (24 mm chord) housing the injector lines, which terminated in a shaped injector nozzle with side cut-outs designed to disperse particles rapidly into the mainstream. This nozzle is identical to the geometry used for the calibration experiment reported in Ref. [10]. The velocity ratio of the streak was set at 3:1 to produce vigorous turbulent mixing with the main flow. Downstream of the injector, nine rows of mixing pins were placed across the channel in three sets of three. Each set contained two staggered rows of pins spanning the channel in the H direction, followed by one row of long pins in the $2H$ direction, with a single short pin across the center for support. The pins were 2.1 mm wide and thick, and the center-to-center distance between pins was 5.4 mm within-row and 8.6 mm between rows.

The particle-laden flow then entered the louvered separator test section. The separator design followed the basic specifications of Ref. [5] for a case with $N = 8$ ribs, an AR = 1.5, and a fixed louver angle $\theta = 340$ deg. However, modifications were made to the louver and collector designs to ensure compatibility with MRP requirements. The initial louver thickness was chosen to be 1 mm. However, deflection of the louvers due to the flow was of concern because the model was fabricated in plastic. To prevent deflection, a 1.6-mm diameter circular cylinder was overlaid on the top of each louver, and a triangular prism was added to the

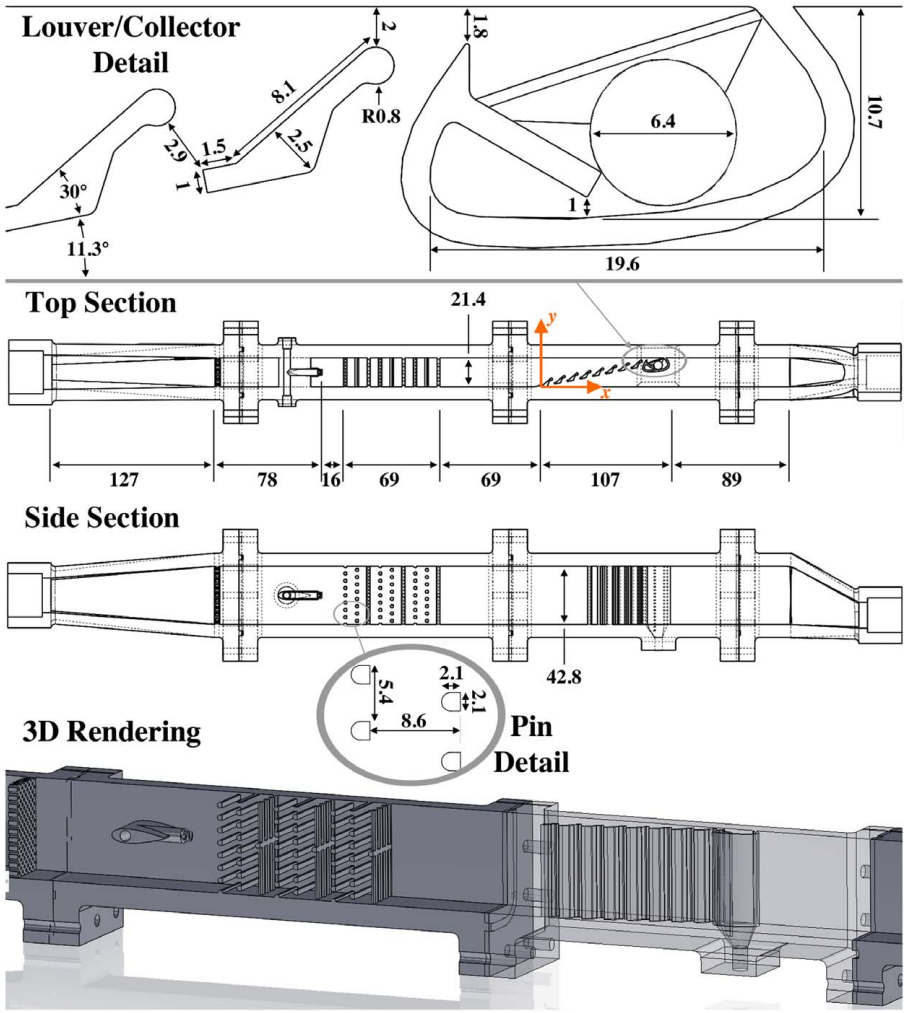

Fig. 2 Separator geometry used for the present work. From bottom to top: 3D rendering of the full geometry; cut section viewed from the side; cut section viewed from the top, with coordinate origin shown (origin is in channel symmetry plane); detail view showing collector and louver design

lower back, increasing the maximum thickness of each louver to 2.5 mm. Neither addition modified the upstream face of the louver, which was assumed to be the most important geometric feature for separating the particles. However, the rounded tip did reduce the minimum flow area between louvers by 17%, giving the geometry an actual area ratio of 1.1. Flow passing through the louvers continued around the collector, through an 89 mm length of straight channel and finally through a contraction to a 19 mm (3/4 in.) diameter circular cross section exit opening.

The collector was designed to match the "wedge and baffle" geometry of Ref. [6] as closely as possible. However, particles in an MRP experiment do not form deposits on the channel walls and an MRP experiment requires data acquisition under steady-state conditions for nearly an hour. Thus, allowing particles to accumulate in the collector would be both undesirable and not representative of the actual deposition physics in an airflow channel. To account for this, one side wall of the collector was replaced with a lofted connection to a 6.4 mm (1/4 in.) diameter tubing barb, allowing the collector flow to be drained continuously. The channel was always oriented with the drain at the bottom so that gravity would help to carry particles out of the collector. The maximum drain flow was set by the channel design, and found to be around 5% of the total Q. Flow through the collector drain could also be metered down or completely shut off by a drain line valve. For the present set of experiments the drain flowrate was fixed at $0.03Q$, which was chosen to balance two competing concerns: minimizing the transverse flow in the collector (which required slower draining) and providing sufficient flow to prevent particles from settling out in the drain lines.

Magnetic Resonance Imaging Techniques. Two MRI-based techniques were employed. The first technique, known as magnetic resonance velocimetry (MRV), provides the mean, 3D, three-component velocity field everywhere in the flow [12]. MRV measurements are made with no particles present. The second technique is known as magnetic resonance particle (MRP) concentration. This method works by measuring the local MRI signal decay rate in the presence of titanium microparticles approximately 30 μm in diameter. The decay rate is linearly proportional to the particle volume fraction, ϕ_V [13]; MRP thus provides the full, 3D mean particle concentration distribution for two-phase systems. Recent publications by Borup et al. provide complete details of the MRP development, as well as its applicability to other particle-laden flows in turbomachinery [9,10].

The full procedure for obtaining MRV/MRP data was as follows. All data were acquired in a single session using a clinical-grade, 3T MRI magnet (GE Healthcare). First, the flow loop was filled with 0.06 M copper sulfate aqueous solution and placed in the MRI magnet. The particle feeder was also filled and connected, but initially blocked from the main flo4w loop by a valve. Velocity data were acquired using MRV on a $0.68 \times 1.0 \times 0.70$ mm grid in the (x, y, z) directions, respectively (the coordinate system is shown in the "Top Section" view of Fig. 2, with the origin located in the channel symmetry plane). The 3D, three-component velocity field was acquired repeatedly for both flow-on (24 measurements) and flow-off (7) cases. Averaging over repeated measurements reduced random noise from the MRI hardware and flow, while subtraction of the flow-off data corrected for measurement bias. Next, water was added to the system to reduce the copper sulfate concentration to 0.01 M, the appropriate value for MRP. The signal decay rate was measured twice: first with no particles present (averaging over 60 measurements) and with particles (30). The difference in decay rate at each point was then converted to particle concentration, producing the full ϕ_V distribution (as described in Ref. [10]). The 95% confidence interval for velocity data was approximately $\pm(0.1, 0.04, 0.02)U_{bulk}$ in (x, y, z), while the confidence interval for ϕ_V values ranged from $\pm 0.006\%$ (in the low-turbulence inlet region) to $\pm 0.075\%$ (in the high turbulence downstream of the louvers), for a signal-to-noise ratio (SNR) of approximately 8 at the bulk ϕ_V.

Table 1 Separation efficiency compared with previously published results

	Study	Re	Mean Stk	η
1	Musgrove et al.	8000	0.9	0.42 ± 0.32
2	Musgrove et al.	15,000	1.6	0.30 ± 0.02
3	Sim et al. (2017)	20,000	0.033	$0.01^{+0.14}_{-0.01}$
4	Sim et al. (2018)	33,300	0.068	0.16 ± 0.14
5	Sim et al. (2018)	33,300	0.068	0.31 ± 0.10
6	Present	8600	0.015	0.065 ± 0.007
7	Present	17,100	0.030	0.087 ± 0.003

Flow Parameters. Particles were supplied from the feeder described in Ref. [9]. For the MRP experiments, the feeder was filled to 4% particles by volume. The particle supply was then diluted to the desired $\phi_{V,inj} = 0.86\%$ upstream of the flow model and injected into a clean main flow. The streak provided 5.8% of the total flowrate, so that the bulk ϕ_V upstream of the separator geometry was 0.050%. For the non-MRI efficiency experiments, these three concentrations were reduced to 1.6%, 0.34%, and 0.02%, respectively, with the streak providing the same portion of the total flowrate to ensure identical flow physics. The primary difference between the present flow and previous studies was the presence of *two* outlet streams: the main outlet and the particle collector drain. Flow out of the collector was controlled via a non-intrusive, clamp-on valve placed on the drain line and always held at 3% of the total flowrate through the separator. All flowrates in the experiments were monitored using four ultrasonic flow probes (Transonic Systems, Inc.). Particles flowing through the drain line did not affect the flowmeter reading.

The Reynolds number for the flow was defined based on the bulk velocity and channel height. Overall particle separation performance was measured for two cases: $Re = 17$, 100 and 8600. These corresponded to bulk flow velocities $U_{bulk} = 0.8$ and 0.4 m/s, respectively. Both Reynolds numbers were within the range of values tested by Musgrove et al. [6], but below those studied by Sim et al. [7,8]. Three-component mean velocity data were also obtained for both cases using MRV. Even *mean* local velocities in this flow approach $3U_{bulk}$, which led to significant artifacts in the high-Re case. Strong turbulence also significantly lowered the achievable MRI SNR downstream of the louvers. For these reasons, MRV data are only reported for the low-Re case, and MRP measurements were only made at low Reynolds number. The particles used were titanium microspheres with a mean diameter of 33 μm, identical to those used in all previous MRP experiments (Ti6Al4V Grade 23 alloy, LPW Technologies). The Stokes numbers (reported later, in Table 1) for these particles were small compared to the range expected in an actual turbine engine. However, these titanium particles are the only type for which MRP has been validated to date. The particles were dynamically similar to particles with $d_p \approx 5$ μm in the Musgrove et al. and Sim et al. experiments, allowing for a cross-experiment comparison and ensuring relevance to turbine engine designers.

Results and Discussion

Separator Performance. A particle separator test was performed in lab (i.e., not in an MRI setting) over a total run time of 50 min. First, high-Re conditions were reached and the flow was inspected visually. Particles entering the collector were observed never to bounce back into the main flow. Next, four 15-s samples were taken from the drain over a 10 min period (to capture any drift). A 15-s sample was also obtained directly from the feeder to provide a reference particle concentration. The flow loop was

then switched to low-Re conditions, and four 30-s drain samples were taken over another 10 minperiod. A final feed sample was obtained under low-Re conditions. The samples were analyzed by first finding the total weight of the particles and water, then pouring the sample through a filter to obtain the dry weight of particles. The resulting weights were used to calculate ϕ_V for each sample.

Overall performance was quantified with the separation efficiency, η, commonly employed in the literature. For this experiment, the efficiency was computed as

$$\eta = \frac{Q_{\text{drain}}\phi_{V,\text{drain}}}{Q_{\text{in}}\phi_{V,\text{in}}} \tag{1}$$

where the fluxes, Q, were known from flowmeter readings, ϕ_V, drain was measured from samples taken from the collector drain line, and ϕ_V, in was computed from the Q values and measured ϕ_V from the feeder output samples. Other metrics are available based on the measurement technique used. For example, Musgrove et al. [6] used the *mass* ratio of collected sand to total sand entering the separator, which is identical to the above definition for particles of constant density. Meanwhile, Sim et al. [8] computed the efficiency as

$$\eta = 1 - \frac{Q_{\text{downstream}}C_{\text{downstream}}}{Q_{\text{upstream}}C_{\text{upstream}}} \tag{2}$$

where C represents the particle *number* density. This definition only matches the previous if all particles have the same diameter. Sim et al. addressed this problem by using an optical probe to obtain simultaneous measurements of C and d_p, then computing η separately for nine bins of roughly constant particle diameter.

The results of the present experiment and earlier studies are reported in Table 1. Particle diameters are given as the mean and approximate 95% range of the volume-weighted diameter distribution for the present and Musgrove et al. results, and as the approximate bin range for both Sim et al. studies. Stokes numbers were computed from U_{bulk}, δ, and the mean d_p in all cases. The mean separation efficiency is reported in the final column: a 95% confidence interval is provided for the present and Musgrove studies, while the plus/minus intervals for the Sim et al. cases are taken from their figures (the definition of the interval was not provided).

Results from the earlier studies are mixed. Collection efficiencies ranged from 0.01 to 0.42. The mean η for the MRI-compatible separator was measured with higher confidence than in the previous studies. The efficiency increased by a factor of 1/3 when the Reynolds number (and Stokes number) were doubled, but overall η values were low compared to earlier results. The only cross-study comparison available at similar Stokes number is between cases 3 and 7: the separation efficiency, η, was much higher for the present design (case 7), but the value was within the large uncertainty range reported by Sim et al.

Figure 3 shows η for all studies plotted against both Re and Stk. No clear trend is present for the Reynolds number scaling, but there does appear to be a positive correlation between η and the Stokes number that is well described by an $\eta \propto \log(\text{Stk})$ relationship. However, cases 2 and 5 had the same η despite a 24 × difference in Stk. As mentioned previously, the 2 × difference in efficiency between cases 4 and 5, which had the same geometry, highlights the importance of the collector characteristics: the only difference between the two cases is that the interior collector walls were greased for case 5, causing more particles to stick instead of bouncing out.

To summarize, the MRI-compatible separator allowed 6 to 9% of particles to be removed from the channel on only 3% of the total flow. These results were within the range of results reported in previous studies. Doubling the Reynolds number doubled the particle Stokes number and led to a 1/3 increase in separation efficiency in the current set of experiments. Higher Stokes number was also correlated with improved separation efficiency when comparing across studies, as indicated by the rough trendline in Fig. 3(*b*). However, this final claim should be considered carefully in light of the high uncertainty in previous results and wide variation across studies; further experiments with carefully controlled geometry, inflow, and boundary conditions are needed to confirm and (potentially) quantify this trend.

In terms of practical use, an O(10%) reduction in bulk ϕ_V is unlikely to mitigate particle damage in a turbine engine. Real engines likely have higher Re and Stk values than measured here, which would be expected to increase the efficiency. Increasing the percentage of drained flow could also improve η, but at the cost of reducing the available flow for cooling. Regardless of whether the present design is efficient enough for filtering an aircraft secondary air stream, it serves as a useful test case. The 3D velocity and concentration data that follow provide insights into the multiphase flow physics and are used to suggest future design improvements.

Particle Transport. Analysis of the MRI data begins with the flow conditions upstream of the particle separator. Figure 4(*a*)

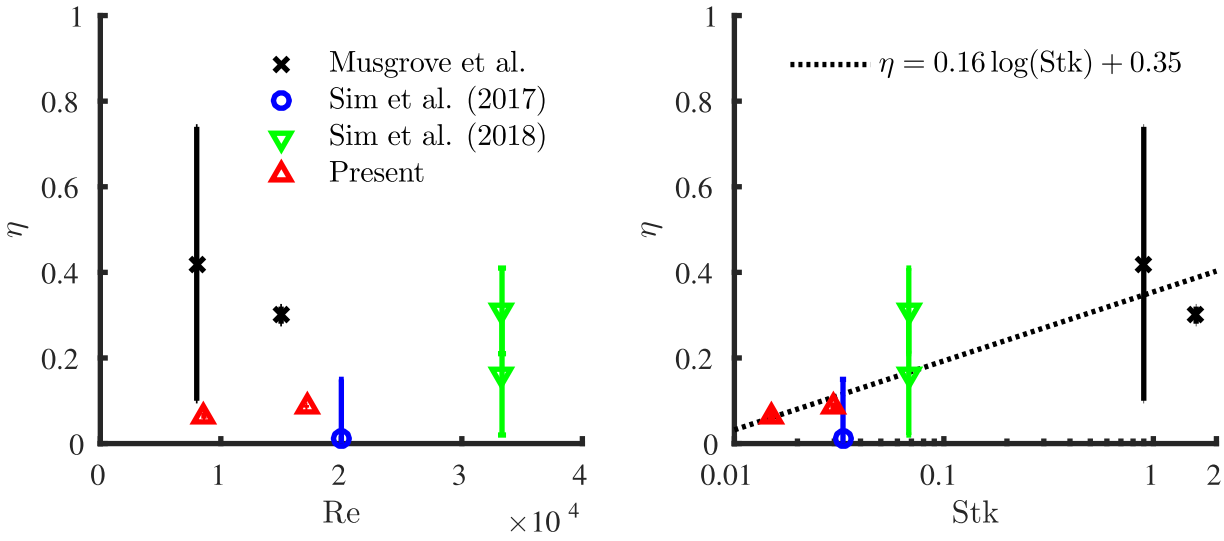

Fig. 3 Separation efficiency for all stuides plotted against Reynolds number (L) and Stokes number (R)

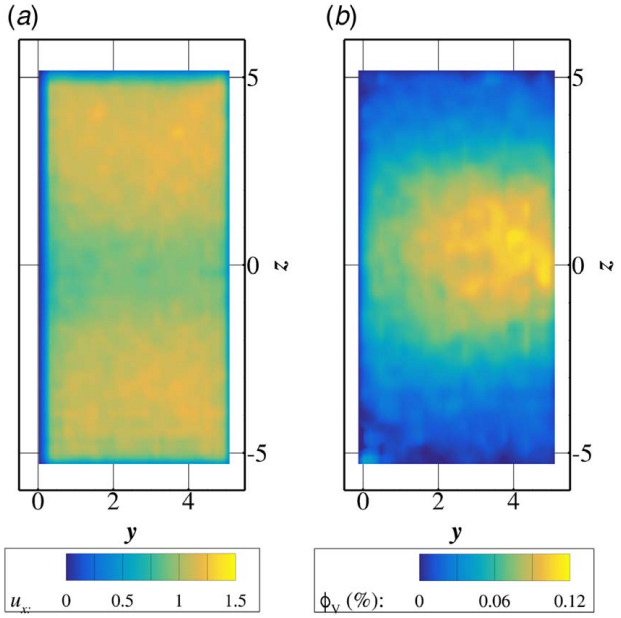

Fig. 4 Contours of (*a*) streamwise velocity (u_x) and (*b*) particle concentration (ϕ_V) for the $x = -3$ plane just upstream of the first louver

shows the streamwise velocity distribution (normalized by U_{bulk}) for the $x = -3$ plane. This plane is located just upstream of the leading edge of the first louver, which lies along the left wall ($y = 0$). The flow profile is fairly uniform, but a small velocity deficit (around $0.2U_{bulk}$) remains at $z = 0$. This deficit is a result of the short support pin in the mixing pin array. The average in-plane velocity magnitude was measured in the region $-9 \le x \le -3$ and found to be less than $0.03U_{bulk}$, indicating that secondary flows were minimal just upstream of the separator.

Figure 4(*b*) shows contours of ϕ_V for the same plane at $x = -3$. The mixing pins act to spread some particles across most of the channel, but the distribution is nonuniform, with concentrations ranging from 0.12% in the channel center to nearly 0 at $z = \pm 5$. The particle cloud is also off-center in the y direction, centered slightly closer to the collector side ($y = 5$). The nonuniform, off-center particle cloud may have produced slightly higher separation efficiency than would be expected for a uniform distribution.

Wall-normal concentration profiles of ϕ_V in the $x = -3$ plane are shown in Fig. 5. The peak concentration region lies at around $3 \le y \le 5$ for all profiles, although the distribution is flatter farther away from the centerline. The region from $z = -0.9$ to 1.8 may be considered the "core" of the particle cloud, as all y profiles are fairly similar in this region.

The centerplane flow pattern in the separator itself is reported in Fig. 6. Three contour plots are provided to show each velocity component independently. An uneven distribution of flow between the eight louver gaps is immediately visible: both u_x and u_y monotonically increase in magnitude for successive gaps, and u_x gradually increases above the louvers, indicating excess flow. The lack of *any* flow through the first gap is particularly noteworthy. The only exception to the monotonic increase is the last gap, just before the collector, which has an opening smaller than δ. Spanwise velocities are nearly zero everywhere, as one would expect for the channel symmetry plane, but there are two exceptions. In the center of the collector, $u_z < 0$ due to flow proceeding toward the drain. The spanwise velocity is weakly positive in the rib gaps, particularly the last gap at $x = 18$. This indicates that the flow may be weakly asymmetric, perhaps due to a spanwise pressure gradient formed by the drain or due to asymmetry in the streamwise vortex pair (discussed later).

While the flow is mostly two-dimensional, wall effects do occur where the louvers intersect the side walls. The result is the formation of a pair of longitudinal vortices downstream of the louvers, one along each wall. Figure 7 shows an oblique view of the channel, with isosurfaces of Q-criterion, to highlight these swirling flow structures. The Q-criterion uses the second invariant of the velocity gradient tensor, which can be computed as

$$Q = \frac{1}{2}\left(\|\boldsymbol{S}\|^2 - \|\boldsymbol{\Omega}\|^2\right) \tag{3}$$

where $\boldsymbol{S} = \frac{1}{2}(du_i/dx_j + du_j/dx_i)$ is the symmetric rate-of-strain tensor and $\boldsymbol{\Omega} = \frac{1}{2}(du_i/dx_j - du_j/dx_i)$ is the antisymmetric rotation rate tensor [14]. Q values have been normalized by $(U_{bulk}/\delta)^2$ to match with the velocity and length normalizations used in this

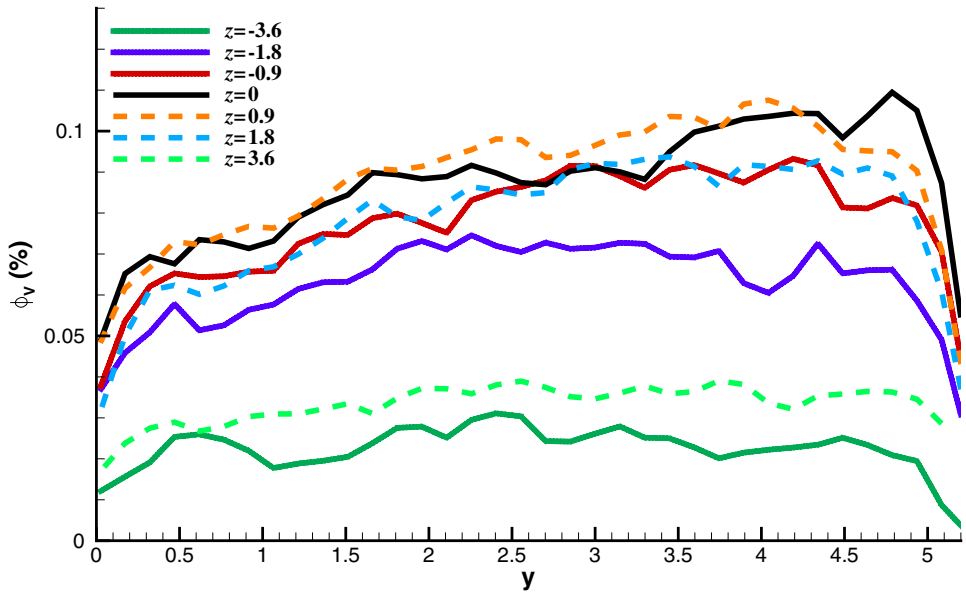

Fig. 5 Wall-normal (y) profiles of ϕ_V at $x = -3$. Shading corresponds to absolute spanwise position, while line pattern indicates $+z$ or $-z$ side of channel

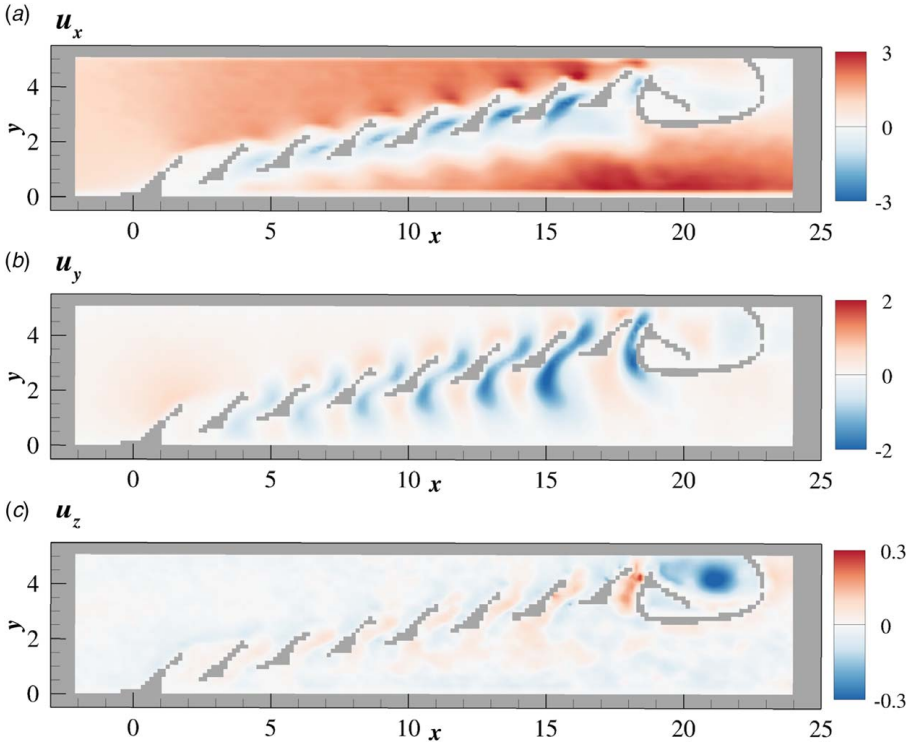

Fig. 6 Contours of (*a*) u_x, (*b*) u_y, and (*c*) u_z in the $z = 0$ plane through the louvers and collector. All velocities normalized by $U_{bulk} = 0.4$ m/s

experiment. Vortices are often defined as connected regions where $Q > 0$. In Fig. 7, the isosurface is drawn at $Q = 1.5$, and the Q field has been smoothed to reduce small-scale noise. The Q isosurfaces are colored by normalized helicity, H, defined as $H = \vec{u} \cdot (\nabla \vec{u})/(U_{bulk}^2/H)$.

Regions with large positive or negative H have vorticity aligned with the flow direction, producing corkscrew-like streamlines. Such regions appear along the side walls due to end effects—the large vortex pair described earlier is readily apparent, but smaller helical regions are also present along the upstream endwall junction of the last few louvers. Meanwhile, high-Q structures with $H \approx 0$ are present behind each louver. In these structures, the vorticity is in the z direction, and $u_z \approx 0$. In other words, each structure represents a swirling separation zone behind a louver. There are actually two disparate $Q > 1.5$ regions per gap: the first shed off of the $+x/+y$ edge of the louver, and a second shed off of the $-x/-y$ edge by flow through the gap turning back in the $+x$ direction. The first structure is responsible for separating particles from the main flow before they can pass between the louvers.

In Fig. 8, contours of ϕ_V are shown for three spanwise planes: $z = 0$, $z = 3.6$, and $z = -4.5$. Incident concentrations are around 0.1% to 0.15% in the centerplane and lower in the side planes. The collector, which will be discussed in detail shortly, contains ϕ_V levels from 0.05% to >0.16% at all spanwise locations. The effect of the louvers is readily apparent, particularly in the centerplane: particles that *do* make it through a gap do so by remaining outside the separation bubble, hitting the upstream face of the next louver, and flowing backward through the gap. This confirms that the acceleration between louvers is too weak to detach most of the particles from the flow, leading to the low η for this design.

The inefficient performance of the louver gap farthest upstream is also clear from Fig. 8. Particles carried into this gap by turbulence enter a region of quiescent flow, allowing them to settle to the $-z$ wall due to gravity. After completely settling out, the particles are only resuspended by sweeps of high-speed fluid penetrating the boundary layer. The $z = 0$ and $z = 3.6$ slices both show high-ϕ_V regions in the first gap where the particles are accumulating and settling, and the large $\phi_V > 0.16\%$ zone in the bottom panel is the

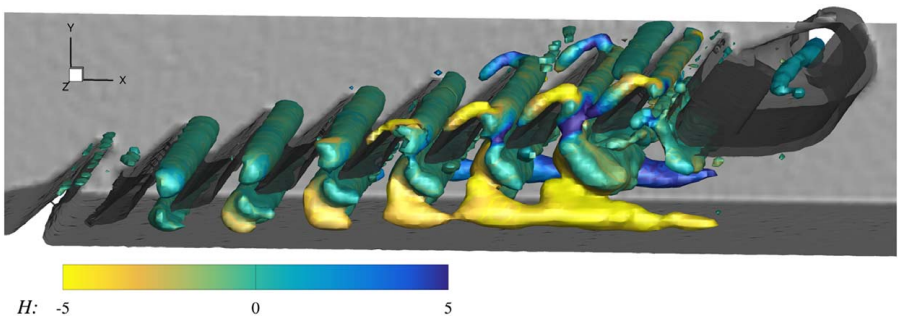

Fig. 7 3D isosurfaces of $Q = 1.5$ (normalized by $(U_{bulk}/\delta)^2$), shaded by normalized helicity, H

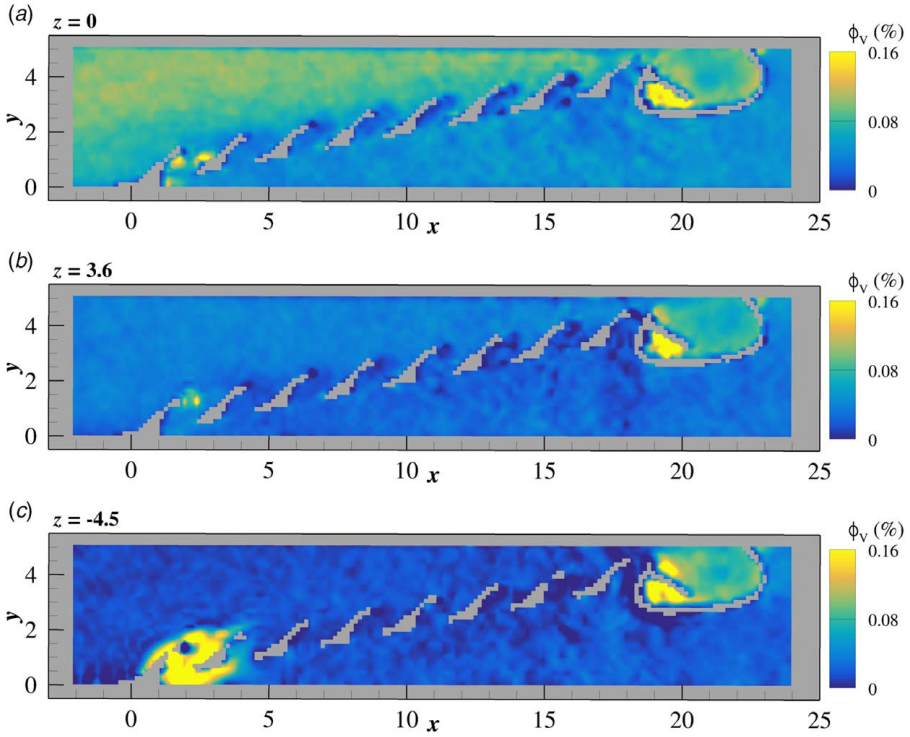

Fig. 8 Contours of ϕ_V in three spanwise planes: (*a*) $z = 0$, (*b*) $z = 3.6$, and (*c*) $z = -4.5$

signature of a bolus of particles lying along the bottom wall. Data within the bolus itself are likely unreliable due to concentrations in excess of 1%.

The louvers also redistribute the particles from the inhomogeneous streak to a uniform distribution across the channel. This phenomenon is visible in Fig. 9, which shows contours of ϕ_V on planes perpendicular to the main flow at the first louver ($x = 0$), through the collector ($x = 21.5$), and downstream of the separation geometry ($x = 27.5$). In the downstream plane, particles are uniformly distributed across the channel, with only a slight excess in ϕ_V visible in the center. The center view of the figure again highlights the elevated concentrations found throughout the collector.

The separator efficiency, η, can be computed from the MRV/MRP by examining the bulk normalized concentration flux, $\dot{\phi}_V$, at various locations. This quantity is defined as

$$\dot{\phi}_V = \frac{1}{Q}\iint_A \phi_V(\vec{u}\cdot\hat{n})dA \tag{4}$$

where Q is the volumetric flowrate through a plane A crossing the flow. $\dot{\phi}_V$ at the inlet was found to be 0.050%; this was based on the measured flowrates and feeder samples taken between MRP scans. Elsewhere, $\dot{\phi}_V$ was measured using the MRP data as 0.036% at the main exit ($26 \le x \le 27.5$), and 0.082% at the collector exit ($5.5 \le z \le 7$). Two potential methods for finding η show disagreement. Using the inlet and drain concentrations, via $\eta = (Q_{drain}\dot{\phi}_{V,drain})/(Q_{in}\dot{\phi}_{V,in})$, yields $\eta = 0.05$, which is in fair agreement but slightly underpredicts the sample-based measurement at low-Re. Using the inlet and main outlet yields $\eta = 0.31$, a 4.5× over-prediction. This suggests that measured ϕ_V values were too low in the outlet portion of the channel. The inlet-outlet measurement, computed as $\eta = 1 - (Q_{out}\dot{\phi}_{V,out})/(Q_{in}\dot{\phi}_{V,in})$, also suffers from noise amplification, especially at low η when the two concentrations are fairly similar. For this reason, the direct approach using inlet and drain concentrations is preferred over analysis using MRP data near the ends of the channel.

Finally, previous work has highlighted the importance of collector design and the associated flow pattern inside the collector. Figure 10 shows a magnified view of the flow and particle distribution for three planes in the collector: $z = 0$, 3.6, and −4.5. The left column contains contours of u_z, while the right column shows ϕ_V. All images have in-plane velocity vectors overlaid.

The main collector cavity contains a clockwise vortex at all locations. The sense of this vortex is critical to particle retention in the separator, as observed by Musgrove et al. [6], who reported the presence of a counter-clockwise swirl for some collector designs. Musgrove et al. theorize that a clockwise vortex tends to keep particles inside the collector, while a counter-clockwise swirl can eject particles out along the $+y$ wall. Spanwise flow toward the drain ($u_z < 0$) is visible in the vortex core at all locations, while u_z varies from

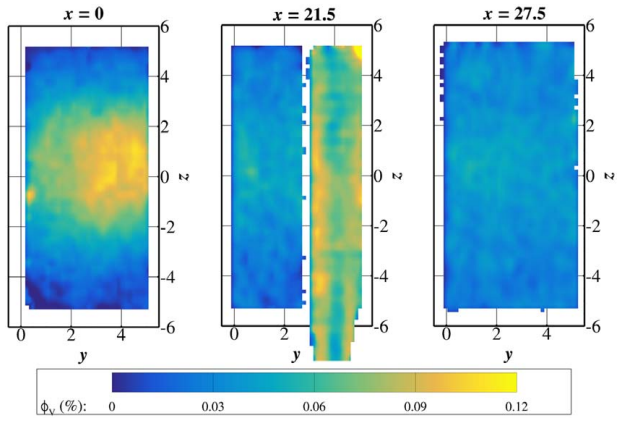

Fig. 9 Contours of ϕ_V for three planes at $x = 0$ at the first louver (L), $x = 21.5$ cutting through the collector (C), and $x = 27.5$ downstream of the separator (R). Note that the center slice includes the collector wall (white region at $y \approx 3$) and data inside the drain tube protruding below the bottom channel wall at $z = -5.5$

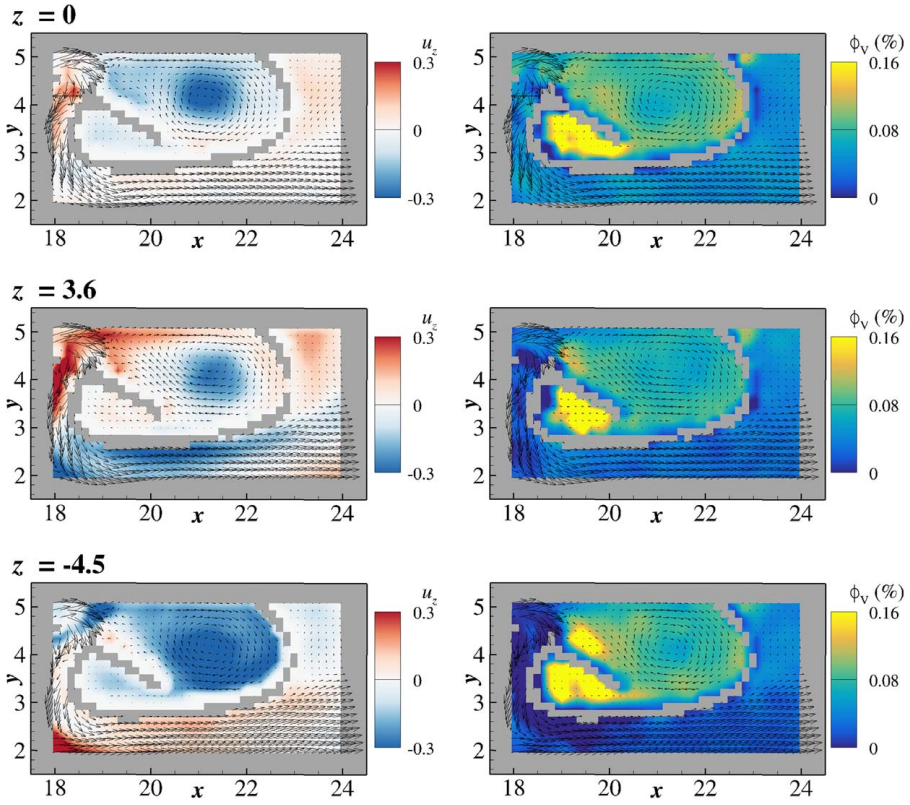

Fig. 10 Detail of flow and particle transport in the collector. Contours of u_z (left row) and ϕ_V (right) with in-plane velocity vectors at three spanwise locations

positive to negative around the edges depending on spanwise position. Meanwhile, the smaller cavity under the inlet lip contains very little in-plane flow, and weaker spanwise velocities than the main vortex.

The particle transport patterns are fairly similar across all three planes. As one would expect, particles inside the collector tend to be centrifuged away from the center of the main vortex, visible as low ϕ_V levels at the core. This is similar to the physics of commonly used swirl-type particle filters. An even more pronounced effect is the tendency for particles to accumulate in the small cavity, where $\phi_V > 0.16\%$ almost everywhere. Particles enter this cavity through the small opening between the collector lip and wall at $(x, y) \approx (20, 3)$. Once there, there is little flow available to carry them back out to the main collector opening. In this sense, the collector can be thought of as a "two-stage" design: first, particles are directed from the main flow into the collector by the louvers; second, many of these particles are spun toward the side wall by the main vortex until they pass into the small cavity, where they can settle out to the drain without further disturbance.

Conclusions

A collector based on the design of Musgrove et al. [5,6] was fabricated for study with two MRI-based techniques: MRV, which provides the 3D, three-component mean velocity field in a single-phase flow; and MRP, a newly developed technique that provides the full 3D concentration distribution for a dispersed phase of solid microparticles. The separator design was modified slightly from previous studies, with the primary change being the addition of a drain on one side of the particle collector, since the titanium particles in water flow (required for MRP) do not stick to the walls. For all experiments, 3% of the total flow was extracted through the collector drain. The overall particle separation efficiency, η, was measured by sampling the inlet and drain flows with the separator running outside of the MRI environment. The measured efficiency was poor, ranging from 6% to 9% at the two Reynolds numbers studied. These results are within the range of previous measurements. A Stokes number based on the inter-louver gap, δ, provided a possible scaling for seven η measurements taken across four studies. It is difficult to draw further conclusions due to large measurement uncertainty and variation across studies; however, this difficulty itself provides evidence that the separation efficiency is sensitive to both geometry and flow conditions.

MRV and MRP were used to analyze the flow and particle transport physics through the collector. Flow was observed to be unequally distributed through the louvers, with no flow passing between the first and second louvers. This quiescent region allowed a bolus of particles to accumulate along the bottom wall in the first gap. A strong spanwise vortex was produced downstream of all other louvers, but most particles were able to follow the flow streamlines closely enough to pass through the gaps, even after impacting the upstream face of the next louver. The separation efficiency measured using MRP data was in fair agreement with the direct sample measurements. The collector design appeared to work very well despite the poor overall performance. A strong vortex was produced in the desirable direction (identified by Musgrove et al.) inside the collector. Particles entering the separator were mostly retained by centrifugation toward the collector walls and into a smaller cavity with quiescent flow conditions. Improvement of the overall η could be achieved by removing the first louver gap altogether, and modifying the remaining louvers to produce an equal flow through each gap—one approach would be the variable louver angle arrangement of Musgrove et al., which was not considered in this study.

The MRI data for this geometrically complex and application-relevant flow will be made available upon request to other

researchers for use in CFD validation. Meanwhile, future experimental work should focus on exploring a wider range of Stokes and Reynolds numbers. It will be critical in all future studies (experimental and computational) to maintain a well understood, standardized geometry and well defined inlet and boundary conditions to produce reliable results. Ultimately, the aim of such work will be to develop quantitative design criteria and analysis metrics for separator efficiency; while the present work is a step in this direction, many more studies are needed to provide sufficient data.

Acknowledgment

Research expenses were supported by the National Science Foundation Fluid Dynamics Program under EAGER grant CBET–1662422. Daniel Borup was supported by an Office of Technology Licensing Stanford Graduate Fellowship and a National Science Foundation Graduate Research Fellowship (Grant No. DGE–114747).

Nomenclature

C = particle concentration (various definitions)
H = normalized helicity
Q = normalized Q-criterion (without subscript)
$u_{x,y,z}$ = normalized velocity components
Q_{location} = volumetric flowrate (with subscript)
U_{bulk} = bulk velocity
x, y, z = Cartesian coordinates
η = overall separator efficiency
ϕ_{V} = particle volume fraction
$\phi_{\text{V,inj}}$ = injected particle volume fraction
$\dot{\phi}_{\text{V}}$ = normalized concentration flux

References

[1] Dunn, M. G., Padova, C., Moller, J. E., and Adams, R. M., 1987, "Performance Deterioration of a Turbofan and a Turbojet Engine Upon Exposure to a Dust Environment," ASME J. Eng. Gas Turbines Power, **109**(3), pp. 336–343.
[2] Hamed, A., Tabakoff, W., and Wenglarz, R., 2006, "Erosion and Deposition in Turbomachinery," J. Propul. Power, **22**(2), pp. 350–360.
[3] Kim, J., Dunn, M., Baran, A., Wade, D., and Tremba, E., 1992, "Deposition of Volcanic Materials in the Hot Sections of Two Gas Turbine Engines," ASME J. Eng. Gas Turbines Power, **115**(3), pp. 641–651.
[4] Dunn, M. G., 2012, "Operation of Gas Turbine Engines in an Environment Contaminated With Volcanic Ash," ASME J. Turbomach., **134**(5), p. 051001.
[5] Musgrove, G. O., Barringer, M. D., Thole, K. A., Grover, E., and Barker, J., 2009, "Computational Design of a Louver Particle Separator for Gas Turbine Engines," ASME Turbo Expo 2009: Power for Land, Sea and Air, Orlando, FL, June 8–12, pp. 1313–1323.
[6] Musgrove, G. O., Thole, K. A., Grover, E., and Barker, J., 2013, "Performance Measurements of a Unique Louver Particle Separator for Gas Turbine Engines," ASME J. Eng. Gas Turbines Power, **135**(1), p. 012001.
[7] Sim, J.-B., Woo, S.-H., Kim, W.-G., Yook, S.-J., Kim, J. B., Bae, G.-N., and Yoon, H. H., 2017, "Performance Estimation of a Louver Dust Collector Attached to the Bottom of a Subway Train Running in a Tunnel," Aerosol Air Quality Res., **17**(8), pp. 1954–1962.
[8] Sim, J.-B., Yeo, U.-H., Jung, G.-H., Park, S.-B., Bae, G.-N., and Yook, S.-J., 2018, "Enhancement of Louver Dust Collector Efficiency Using Modified Dust Container," Powder Technol., **325**, pp. 69–77.
[9] Borup, D. D., Elkins, C. J., and Eaton, J. K., 2017, "Transport of Microparticles in a Turbulated Serpentine Passage," ASME Turbo Expo 2017: Turbomachinery Technical Conference and Exposition, Charlotte, NC, June 26–30, ASME Paper No. 63491.
[10] Borup, D. D., Elkins, C. J., and Eaton, J. K., 2018, "Development and Validation of An Mri-Based Method for 3d Particle Concentration Measurement," Int. J. Heat Fluid Flow, **71**, pp. 275–287.
[11] Borup, D. D., Engel, L. E., Elkins, C. J., and Eaton, J. K., 2020, "Transport and Dispersion of Particle-Laden Streaks in a Standardized Human Nasal Geometry," Exp. Fluids, **61**(2), p. 43.
[12] Elkins, C. J., and Alley, M. T., 2007, "Magnetic Resonance Velocimetry: Applications of Magnetic Resonance Imaging in the Measurement of Fluid Motion," Exp. Fluids, **43**(6), pp. 823–858.
[13] Yablonskiy, D., and Haacke, E. M., 1994, "Theory of NMR Signal Behavior in Magnetically Inhomogeneous Tissues: The Static Dephasing Regime," Magn. Res. Med., **32**(6), pp. 749–763.
[14] Hunt, J. C., Wray, A. A., and Moin, P., 1988, "Eddies, Streams, and Convergence Zones in Turbulent Flows," Proceedings of the 1988 Summer Program, Center for Turbulence Research, Stanford, CA, Summer 1988.